Properties of hot-spot emission in a warm plastic-shell implosion on the OMEGA laser system

W. L. Shang,[1,2,3] C. Stoeckl,[3] R. Betti,[2,3] S. P. Regan,[3] T. C. Sangster,[3] S. X. Hu,[3] A. Christopherson,[2,3] V. Gopalaswamy,[2,3] D. Cao,[3] W. Seka,[3] D. T. Michel,[3] A. K. Davis,[3] P. B. Radha,[3] F. J. Marshall,[3] R. Epstein,[3] and A. A. Solodov[3]

[1]*Research Center of Laser Fusion, China Academy of Engineering Physics, Mianyang 621900, China*

[2]*Fusion Science Center, University of Rochester, Rochester, New York 14623, USA*

[3]*Laboratory for Laser Energetics, University of Rochester, Rochester, New York 14623, USA*

(Received 7 August 2017; published 25 September 2018)

A warm plastic-shell implosion is performed on the OMEGA laser system. The measured corona plasma evolution and shell trajectory in the acceleration phase are reasonably simulated by the one-dimensional LILAC simulation including the nonlocal and cross-beam energy transfer models. The results from analytical thin-shell model reproduce the time-dependent shell radius by LILAC simulation and also the hot-spot x-ray-emissivity profile at stagnation predicted by SPECT3D. In the SPECT3D simulations within a clean implosion, a U-shaped hot-spot radius evolution can be observed with the Kirkpatrick-Baez microscope response (the photon energy is from 4 to 8 keV). However, a fading-away hot-spot radius evolution is measured in OMEGA warm plastic-shell implosion because of mixings. To recover the measured hot-spot x-ray emissivity profile at stagnation, a nonisobaric hot-spot model is built and the normalized hot-spot temperature, density, and pressure profiles (normalized to the corresponding target-center values) are obtained.

DOI: 10.1103/PhysRevE.98.033210

I. INTRODUCTION

Two principal approaches (direct and indirect drive) are used with lasers to generate the energy flux and pressure required to drive inertial confinement fusion (ICF) [1]. In the direct-drive approach, a spherical target is illuminated directly with a number of individual laser beams [2,3]. The laser energy is absorbed by the plasma ablating from the imploding capsule and then is transferred into the central low-density region (hot spot). The main advantage of direct drive is the high coupling efficiency of the laser energy to kinetic energy of the shell (hydrodynamic efficiency ~4%–6%). The highest hot-spot pressure achieved in OMEGA experiments is ~56 Gbars with a neutron yield of $\sim 5.3\times 10^{13}$ [4,5]. In the indirect-drive approach, the laser energy is absorbed and converted to x rays by a high-Z hohlraum that surrounds the target [6]. The main advantage of indirect drive is the reduced sensitivity of implosions to short-scale beam nonuniformities [1]. The highest hot-spot pressure achieved experimentally at the National Ignition Facility (NIF) is ~220 Gbars in a so-called high-foot implosion with a neutron yield of $\sim 9\times 10^{15}$ and a corresponding fuel gain of $G_{\text{fuel}} > 2$ [7]. Here the fuel gain is defined as the ratio of total thermonuclear energy production to the total energy delivered to the deuterium-tritium (DT) fuel. In both direct- and indirect-drive ICF, there are acceleration and deceleration phases. The acceleration phase ends when the laser is turned off and the shell starts traveling at approximately constant velocity. Multiple shock reflections off the incoming inner shell and an increase in gas pressure cause the deceleration phase to begin. During the deceleration phase, the compressing material enclosed by the inner shell surface develops into a low-density high-temperature region called the hot spot [8,9].

Since thermonuclear ignition and high-energy gain are the goals of ICF, one would naturally look to neutron yield as the primary measure of implosion performance [10]. The neutron yield depends on the hot-spot conditions. For DT implosions, the neutron yield is [11]

$$Y = \langle\sigma_{\text{DT}}\rangle n_{\text{D}} n_{\text{T}} V t, \tag{1}$$

where Y is the neutron yield, $\langle\sigma_{\text{DT}}\rangle$ is the DT reaction cross section, n_{D} and n_{T} are the D and T densities in the hot spot, respectively, V is the hot-spot volume, and t is the implosion confinement time. As a result, the hot-spot conditions, particularly the temperature ($\langle\sigma_{\text{DT}}\rangle$ is most sensitive to the plasma temperature), play important roles in ICF. Neutron spectra, charged-particle spectra, and x-ray-emission characteristics also depend on hot-spot conditions and can be used to infer them [6,8,10].

Measurements of continuum x-ray emission from the central hot spot of an ICF implosion can be directly related to hot-spot conditions using the relative dependence of continuum spectral emission rates on temperature and density or pressure [12]. It has been reported that the free-free and bound-free emissivities of hot-spot hydrogen and carbon (by mixing) both scale as the square of the hot-spot pressure, with the assumption of a nominal temperature value [13]. In an unstable implosion, a trace amount of shell material mixed into the hot spot can increase the x-ray emission measurably because of the relatively high emissivity per atom of carbon (or other shell materials) without significantly altering the DT concentration and the hot-spot conditions [14]. Consequently, measured hot-spot conditions and mixing mass were measured in both NIF and OMEGA implosions, based on the K-shell line emission of M-shell ionization species of higher-Z shell dopants [15–17]. Dopant line emission indicates mix originating from the doped shell layers only, while carbon continuum emission indicates fuel-shell mix originating from anywhere in the capsule shell. Recently, based on an isobaric

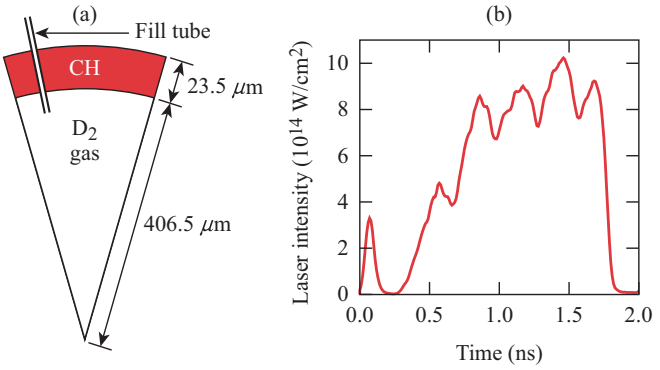

FIG. 1. (a) Target and (b) laser pulse intensity in the experiment. A fill tube of 30 μm outer diameter was used.

implosion, a scaling of the total filtered x-ray emission as a constant power of the total neutron yield for implosions of targets of similar design over a broad range of shell implosion isentropes has been proposed and has been confirmed by experiments [13,14,18,19]. The pressure profile was obtained analytically based on a nominal temperature value, and a near-isobaric pressure was observed [13].

For this work, a warm plastic-shell implosion was performed on OMEGA and the hot-spot emission properties were investigated. The radiative transfer code [20] SPECT3D was used to simulate the hot-spot emission, while the one-dimensional (1D) hydrocode LILAC [21] was used to simulate the hot-spot conditions. In a clean implosion, a U-shaped hot-spot radius evolution was obtained with the Kirkpatrick-Baez microscope (KBFRAMED) response (the photon energy is 4–8 keV). However, in the experiment a fading-away hot-spot radius trajectory was measured, which implies that an unstable implosion with significant mixing is involved. A nonisobaric hot-spot profile was built to recover the measured hot-spot radius. The normalized core pressure, temperature, and density profiles are inferred with this nonisobaric model.

II. WARM PLASTIC-SHELL IMPLOSION ON OMEGA

Figure 1(a) shows the target that was used in the experiment: a 23.5-μm-thick, 430-μm-outer-radius plastic (CH) shell and filled with D_2 gas at a pressure of 15 atm. The capsule was imploded by a 24-kJ relaxation-adiabat shaping UV laser pulse [22], which is shown in Fig. 1(b). The 351-nm-wavelength laser light was smoothed with polarization smoothing [23], distributed phase plates [24], and 1-THz-bandwidth smoothing by spectral dispersion [25]. The shaped pulse comprised an ~80-ps full width at half maximum (FWHM) Gaussian prepulse (picket pulse) and a subsequent near-square pulse. The corresponding nominal laser intensity in the compression portion was $\sim 8\times10^{14}$ W/cm^2. The picket pulse in front of the main pulse launched a shock wave that set the adiabat profile within the shell, which monotonically decreased from the outer ablation surface toward the inner shell surface, and an adiabat of ~3 was achieved when the laser pulse was turned off. A slow-rising main pulse was designed to generate a relatively weak shock to meet the picket shock on the inner surface of the moving shell.

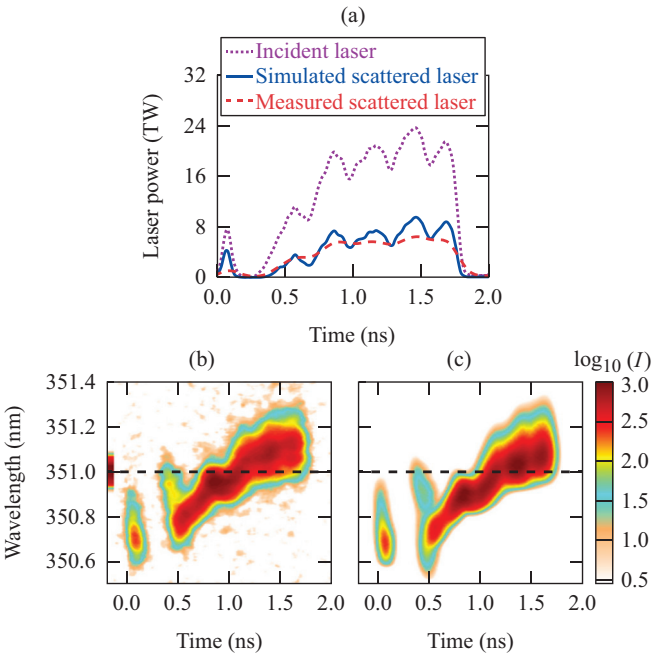

FIG. 2. (a) Measured (by the channel H13B) and simulated scattered light by LILAC and (b) measured and (c) simulated scattered-light spectra.

A 1D LILAC simulation was performed with the measured laser pulse, using the nonlocal thermal conduction and the cross-beam energy transfer (CBET) models [26,27]. Cross-beam energy transfer caused by stimulated Brillouin scattering reduces the absorption, making it possible for incoming light to bypass the highest absorption region near the critical radius. Direct-drive implosions are driven by a rocket effect that is generated by the absorption of laser light at 10^{14}–10^{15} W/cm^2, and CBET significantly reduces the performance of OMEGA direct-drive implosions [28].

Time-resolved scattered-light spectroscopy and time-integrated calorimetry are used on OMEGA to infer the absorption of light by the target [29]. Figure 2(a) compares the measurement (by the channel H13B [29]) and the simulation of the time-resolved scattered-light power. The simulated power (blue line) shows very good agreement with the measured scattered-light power (dashed red line). The LILAC-simulated total laser absorption is 70% and the measured total laser absorption is 68%. Since the light refraction and frequency shift are sensitive to the corona spatial structure, the simulated coronal structure can be validated using time-dependent scattered-light spectral measurements. The simulated spectra [Fig. 2(c)] reproduce reasonably well the basic structure of the measured spectra [Fig. 2(b)] by H13B. However, at the rising phase of the compression main pulse (~0.5 ns), less simulated blueshift is obtained when compared with the measurement, which is attributed to the slower corona plasma expansion in the simulation.

Hot-electron production is an important issue for implosion performance, especially for low-adiabat (α) cryogenic implosions [6], where fuel preheating degrades the hot-spot pressure as $P_s \sim \alpha^{-0.9}$ and the shell areal density as $\rho R \sim \alpha^{-0.54}$ [30]. Hot electrons can be generated by the nonlinear processes of

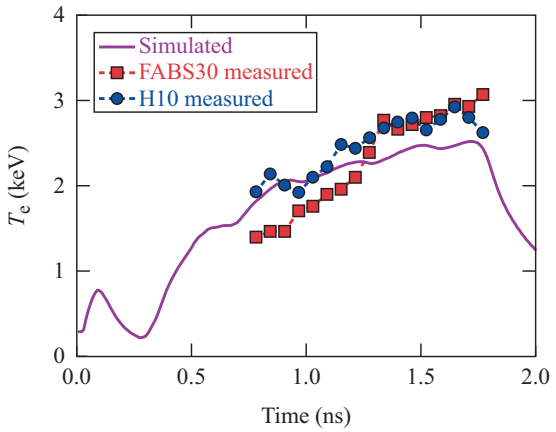

FIG. 3. Simulated and measured corona temperatures at quarter-critical surface in corona plasma.

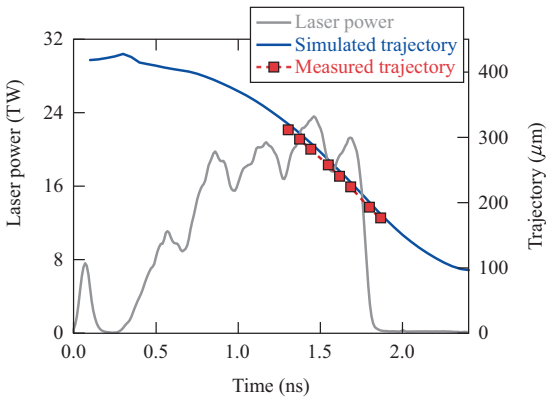

FIG. 4. Simulated and measured shell-ablation-surface trajectories and the laser power pulse.

laser-plasma interactions, including the three-wave parametric instabilities: stimulated Raman scattering (SRS), two-plasma decay (TPD), and filamentation instability, when the laser intensity is (5×10^{14})–(2×10^{15}) W/cm^2 for conventional direct and indirect drive ICF [31,32]. In OMEGA direct-drive implosions, the coincidence of TPD signatures, combined with the absence of SRS-backscattered light, is considered evidence for the dominance of the TPD instability over other potential sources of hot electrons or harmonic emission. The half-integer harmonic spectra measured by the full-aperture backscatter stations (FABSs) can be used to investigate the TPD instability and the corona temperature at the quarter-critical surface can be inferred by the wavelength shift [32,33]. As shown in Fig. 3, the measured corona temperatures at the quarter-critical surface with two different channels (FABS30 and H10) are in very good agreement with the LILAC simulation. As a result, the time-dependent corona plasma conditions, including the expanding and inward movements, can be reasonably modeled by 1D LILAC simulations with nonlocal and CBET models.

A time-resolved, four-channel hard-x-ray detector [34] provides a measurement of the time history of the hard-x-ray emission and hot-electron temperature. In our experiment, the hot-electron temperature was measured to be ~50 keV. A simple formula, balancing bremsstrahlung emission and stopping power for energetic electrons, is used to relate the bremsstrahlung emission E_{br} (total time-integrated spectral emission, in units of keV/keV sr) to the amount of energetic electrons [35]

$$E_{br} = \frac{6.3}{4\pi} \times 10^9 \langle Z \rangle E_{hot}(J) e^{1-h\upsilon/T_{hot}}, \qquad (2)$$

where $\langle Z \rangle$ is the effective atom number, E_{hot} is the hot-electron energy, and T_{hot} is the hot-electron temperature. The measured hard-x-ray energy is ~22.3 mJ, with Eq. (2) the conversion efficiency (E_x/E_{hot}) from hot-electron energy to hard x ray, which can be obtained as ~0.000 61, and the absorbed-laser-to-hot-electron conversion efficiency (E_{hot}/E_a) is ~0.21%, where E_a is the absorbed laser energy. Because of the low E_{hot}/E_a, the preheating caused by hot electrons is not the dominant performance-degradation mechanism in our experiment.

In the experiment, the soft-x-ray emission from a warm plastic target was measured with an x-ray framing camera and used to determine the shell trajectory [36]. The submicron-level accuracy of this method results from using emissivity profile features that do not require Abel inversion to analyze and are insensitive to perturbations of the ablation front [37]. A comparison of the measured shell trajectories with simulations postprocessed to account for the time integration, the spatial resolution, and the filtering of the diagnostic [38] is shown in Fig. 4 and good agreement is obtained, which implies that the acceleration phase in the experiment can be reasonably modeled in the LILAC simulation with the nonlocal and CBET model and the ablation-surface trajectory is independent of the shell perturbation.

The neutron temporal diagnostic was used to measure the neutron rate's history [39]. Figure 5 shows the simulated and measured neutron rates along with the simulated ρR evolution. It also shows that the ρR increases during neutron production and the fusion reactions are quenched near the time

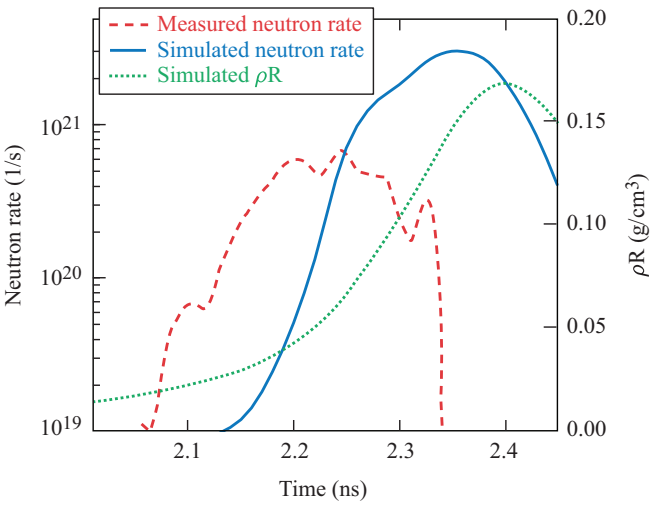

FIG. 5. Comparison of measured neutron rate, LILAC predicted neutron rate, and predicted ρR evolution.

the areal density reaches 0.12 g/cm^2. The measured neutron rate is lower and truncated compared to the 1D simulated fusion rate, likely because of the shell mixing [40]. The shell's outside-surface instabilities grow at the acceleration phase, feed through the shell to its inner surface, and interact with the initial inner-surface perturbations. The shell's inner-surface instabilities grow during the deceleration phase, leading to mixing into the hot spot. The perturbation could degrade the implosion performance, increase the hot-spot size, and decrease the hot-spot pressure and temperature at stagnation [28]. The nuclear reactions could occur earlier compared to the 1D clean implosion because of the compression of the spikes. Therefore, an earlier bang time can be achieved with a lower neutron rate compared to the 1D simulation. These issues are clearly demonstrated in Fig. 5. However, there could be other reasons for the earlier bang time in the experiment, like a higher velocity or a less back pressure at stagnation, and also the ablator may be burned through and lead to unknown confinement at stagnation. Two- or three-dimensional simulation is needed to investigate the hot-spot and shell dynamics at the deceleration and stagnation phases.

III. PROPERTIES OF HOT-SPOT EMISSION IN A WARM PLASTIC-SHELL IMPLOSION ON OMEGA

An analytical model (thin-shell model) [41] was used to investigate the deceleration phase of the warm plastic-shell implosion on OMEGA. This model was derived by solving the conservation equations for the hot spot. The heat flux and the radiation energy leaving the hot spot go back in the form of inertial energy and pdV work of the material ablated off the inner shell surface. Although the hot-spot temperature is reduced by the losses due to heat conduction, the hot-spot density increases because of the ablated material entering the hot spot in such a way that the hot-spot pressure is approximately independent of heat conduction [41]. Consequently, heat conduction and radiation transport are ignored in the model. A formula for the shell trajectory can be obtained in a straightforward manner by this thin-shell model,

$$\hat{R} = \sqrt{1 - 2\hat{t}\hat{U}_0 + \hat{t}^2\left(1 + \hat{U}_0^2\right)}, \tag{3}$$

where $\hat{R}$ is the shell radius normalized to the initial shell radius R_0 at the start of the deceleration phase; $\hat{t}$ is the time normalized to τ_0 with the expression $\tau_0 = [\frac{M_{\text{shell}}}{4\pi P_0 R_0}]^{0.5}$, where M_{shell} and P_0 are the initial shell mass and hot-spot pressure at the start of the deceleration phase; $\hat{U}_0$ is described as $\hat{U}_0 = U_0\tau_0/R_0$; and U_0 is the average shell implosion velocity at the beginning of the deceleration phase. In our warm plastic-shell implosion, $R_0 \sim 128\ \mu$m, $P_0 \sim 0.13$ Gbar, $U_0 \sim 300\ \mu$m/ns, and $M_{\text{shell}} \sim 0.03$ mg, leading to $\tau_0 = 1.2$ ns and $\hat{U}_0 = 2.9$.

Figure 6 shows the evolution of the shell radius (shell mass center) in our implosion according to both the LILAC simulation and the thin-shell model (3) without α heating. Since D_2 gas was used in the target, the no-α-heating hypothesis is quite reasonable. As shown in Fig. 6, very good agreement was obtained in the first 0.1 ns. However, at about 0.12 ns, there

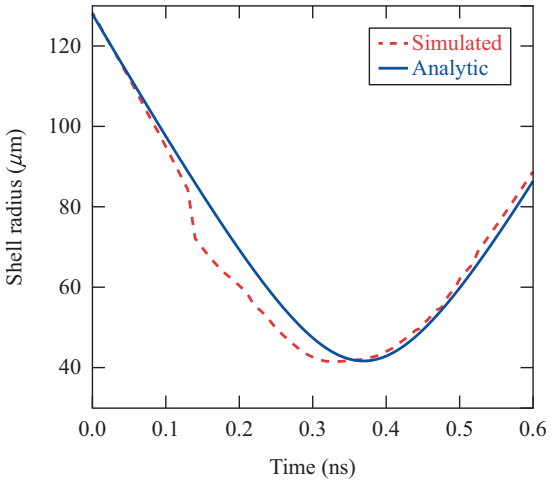

FIG. 6. Evolution of the shell radius by LILAC simulation and thin-shell model without α heating. The start of the deceleration phase (the end of the laser pulse) is 0 ns.

is an inward jump of the shell radius, because the rebound shock collided with the inward-moving shell, leading to a sudden density increase near the shell's inner surface. The rebound-shock shell collision is seen distinctly in the LILAC simulation and is not seen in the analytical thin-shell model. This results in an earlier stagnation time, but the stagnation hot-spot radius is not sensitive to the rebound-shock shell collision.

SPECT3D was used to simulate the target emission from the implosion. Since the KBFRAMED [42] is always used to investigate the hot-spot evolution in experiments, the effect of the KBFRAMED response should be considered within the SPECT3D simulation. The spectral response of the KBFRAMED x-ray camera is shown in Fig. 7(b). The response function is nearly Gaussian in shape with spectral widths of ~1 keV centered at energies near ~5.5 keV [13].

The SPECT3D-simulated hot-spot radius with KBFRAMED response is shown in Fig. 7(a), and the hot-spot radius was chosen to be the 50% falloff location. During the deceleration phase, the hot spot is formed, and the temperature and density in the hot-spot region keep increasing until stagnation. In our SPECT3D implosion simulation, the radius indicated by hot-spot emission is measurable with a radius of 45 μm at ~2.2 ns and the hot-spot radius converges to 22.5 μm at 2.4 ns (stagnation occurs). After stagnation, the target expands and the hot-spot radius increases. As a result, a U-shaped hot-spot radius evolution is formed.

The normalized total x-ray emission (spectrum- and space-integrated) evolution with the KBFRAMED response is shown in Fig. 7(c). As can be seen, the hot-spot emission intensity is nearly Gaussian in shape with the peak at stagnation, although the smallest core size is at stagnation.

The normalized density and T_e profiles by LILAC simulation at stagnation are shown in Fig. 8. The radiation and thermal flux from the hot spot deposit energy at its inner surface and create a step shape in the shell's density profile. In addition, T_e falls from the target center to the hot-spot boundary. Figure 8 also shows the x-ray-emissivity profiles by SPECT3D and the

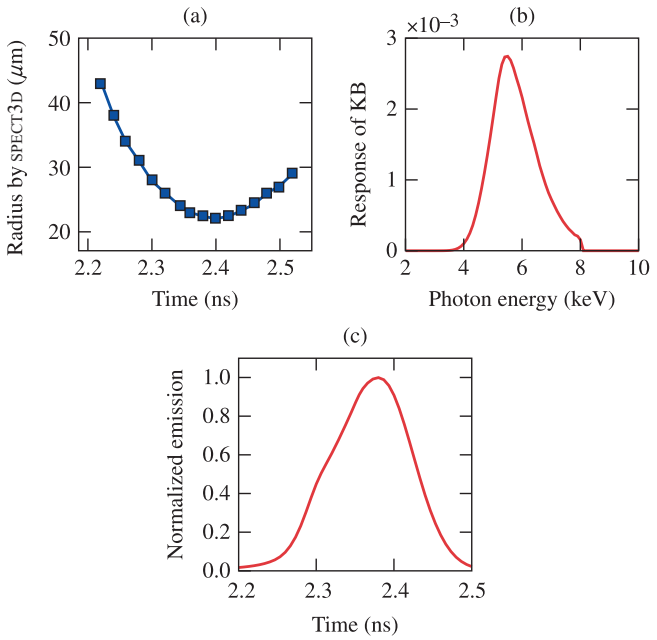

FIG. 7. (a) The SPECT3D-simulated hot-spot radius with the KBFRAMED response (the photon energy is 4–8 keV). (b) The KBFRAMED response. (c) Time-dependent emission of the implosion filtered with the KBFRAMED response.

analytical thin-shell model. As can be seen, the brightest x-ray emission is located at the hot-spot boundary and this feature marks the hot-spot radius in Fig. 7(a). The x-ray emission keeps increasing from the hot-spot center to the hot-spot boundary, reaches a peak at the boundary, and then decreases abruptly because of the low temperature in the shell. The brightest emission intensity at the hot-spot boundary is 1.7× the target center's emission intensity. In the thin-shell model

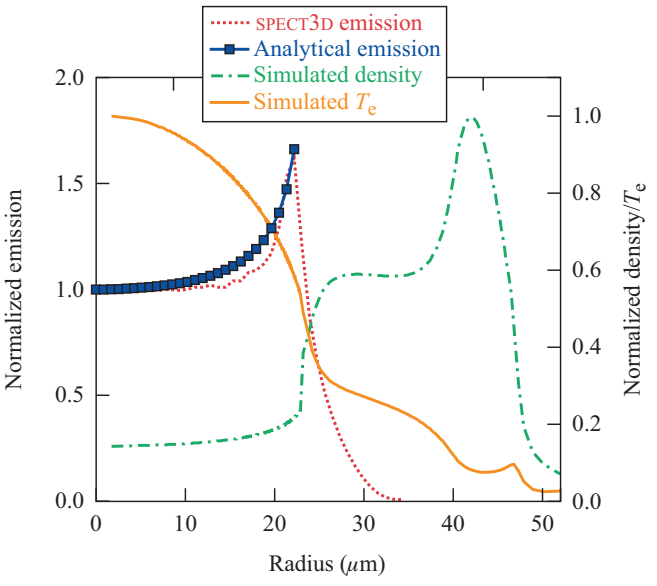

FIG. 8. Normalized profiles of hot-spot density and T_e by LILAC, x-ray emission by SPECT3D, and x-ray emission by an analytical thin-shell model. All the plots are at stagnation.

with an isobaric hot spot, analytical derivations were given for T_e and density profiles in the hot spot as [41]

$$T(\hat{r}) = T_0 \frac{(1-\hat{r}^2)^{0.4}}{1-0.15\hat{r}^2}, \tag{4}$$

$$\rho(\hat{r}) = \rho_0 \frac{1-0.15\hat{r}^2}{(1-\hat{r}^2)^{0.4}+\epsilon}, \tag{5}$$

where T_0 and ρ_0 are the temperature and density in the hot-spot center, respectively, $\hat{r}$ is the position normalized to the hot-spot radius, and ϵ is an *ad hoc* term to remove the singularity at $\hat{r} = 1$. A commonly used hot-spot temperature profile $T(\hat{r}) = T_0(1-\hat{r}^2)$ [43] is in very good agreement when compared with Eq. (4). A simple expression for the bremsstrahlung emissivity [44]

$$I \sim Z^3 n_e^2 T_e^{0.5} \tag{6}$$

is used here to investigate the hot spot's x-ray-emissivity profile. With the profiles from Eqs. (4) and (5), the calculation of normalized analytical x-ray emission shown in Fig. 8 is straightforward. Very good agreement is achieved between the SPECT3D and analytical results and it can be concluded that the hot-spot profiles given by the thin-shell model (4) and (5) and the simple bremsstrahlung emission formula (6) can be reasonably used to investigate the x-ray-emission properties in our warm-plasma implosion.

In the experiment, the 16-channel KBFRAMED in the (4–8)-keV photon energy range [42] was used to measure the hot-spot x-ray-emission evolution. The 17% intensity contour radius R_{17} of the gated x-ray image is related to the hot-spot radius [5,42]. For the shot 84 605, the gate time is ∼30 ps and the spatial resolution is ∼6 μm. A resolution grid was used to obtain the spatial resolution, a line out through a single intensity-corrected image taken through the central 200-μm-wide region, and the measured pattern was compared to the Gaussian-blurred step pattern whose FWHM is 6 μm [42]. Spatially and temporally blurs have been performed over the detector resolution and gate width, and the Kirkpatrick-Baez spectral response [shown in Fig. 7(b)] has also been considered in the postprocedure of SPECT3D simulation. In Fig. 7(a) it has been demonstrated that a U-shaped hot-spot radius evolution should be measured in a clean (or near clean) implosion by a KBFRAMED camera. In our experiment, however, the time-dependent hot-spot radius measured by a KBFRAMED is far away from the U shape. A fading-away hot-spot radius evolution was obtained as shown in Fig. 9. This significant discrepancy is a result of the hot-spot mixing caused by the unstable implosion. A larger hot-spot radius at stagnation was obtained compared to the 1D clean implosion. Figure 10 shows the images of stagnation (shot 84 605) recorded by KBFRAMED with times so assigned from the beginning to the end of measurable core emission. Only seven good signal level images were obtained since the emission was only present during an ∼220 ps time period. It should be noted that the structure could be caused by emissivity variation in space inside the hot spot or it could also be affected by absorption of the cold imploding D_2 plasma surrounding the hot spot. However, the absorption is expected to be small at the average energy of the x rays that formed these images (∼4–8 keV) for the range of areal densities

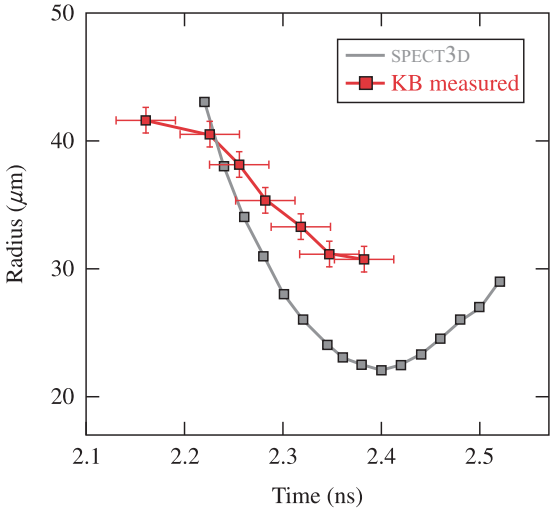

FIG. 9. The SPECT3D-simulated U-shaped hot-spot radius and KBFRAMED measured hot-spot radius (shot 84 605).

expected (~20 mg/cm^2). Therefore, most of the structure should be caused by emission variation in the hot spot.

IV. NONISOBARIC MODEL FOR THE HOT SPOT

To investigate the radial x-ray-emission properties in the implosion, a 2D super-Gaussian fitting was performed for the measured core images. The point-spread function (PSF) smoothed hot-spot image at stagnation is shown in Fig. 11(a), the corresponding super-Gaussian fit is demonstrated in Fig. 11(b), and the measured and fitted intensity profiles taken along the dashed lines through the center of the images are shown in Fig. 11(c) [5,42].

The isobaric state of the hot spot at stagnation is widely used in ICF implosions [13,41,45]. The isobaric hot-spot condition and temperature density scaling of the neutron-production rate explain a scaling behavior of the x-ray yield as a constant power of the neutron yield [13,14,19]. In addition, the isobaric hot-spot profile at stagnation is used to derive the thin-shell model [41] and hydroscalings of the implosion performance [30]. Furthermore, the hot-spot pressure

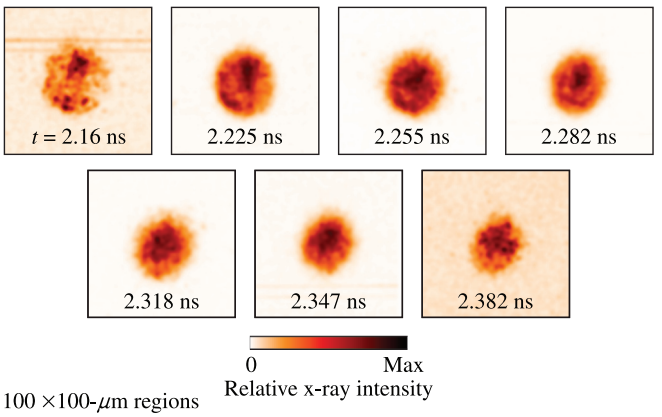

FIG. 10. The KBFRAMED images of hot-spot x-ray emission (shot 84 605).

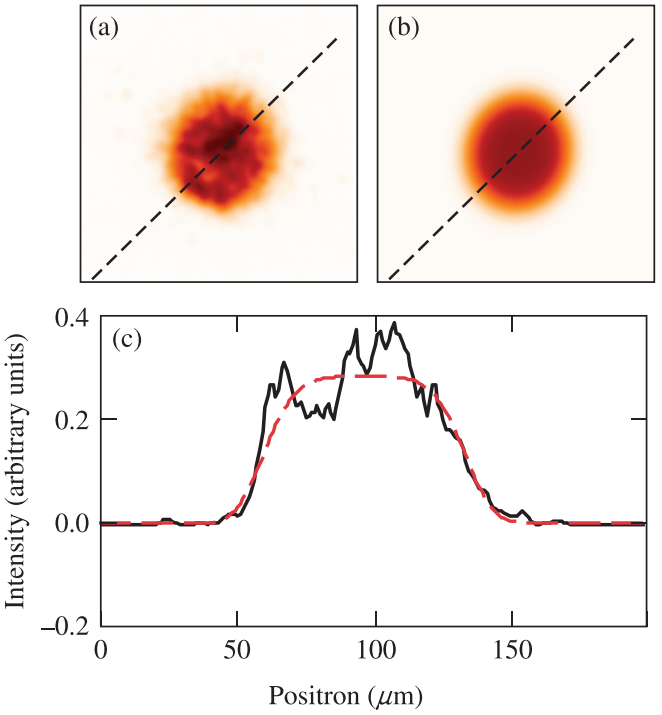

FIG. 11. (a) The PSF smoothed image of the hot spot recorded at stagnation by the KBFRAMED (shot 84 605). (b) Super-Gaussian fit of (a). (c) Measured and fitted intensity profiles taken through the centers of the x-ray images along the dashed lines in (a) and (b).

at stagnation is inferred from x-ray and nuclear diagnostics assuming an isobaric hot spot [5,46]. Within the isobaric hot-spot condition, the x-ray-emissivity profile simulated by the thin-shell model had the brightest emission intensity at the hot-spot boundary, which has been proven by the SPECT3D simulation (shown in Fig. 8). However, the experimental hot-spot emission does not peak at the hot-spot boundary (Fig. 11 and Ref. [5]).

A static model of the core was built to gain additional insight into target performance [47,48]. This model assumed that the compressed core can be divided into two regions: a clean region with only fuel material and a mixed region in which some of the shell material is mixed with the fuel material. The experimental results (primary neutron burn rate, average neutron ion temperature, secondary neutron, proton, and knock-on yields) were compared to the data from the static model [47,48].

It should be noted that the degree of uniformity of mixing in the hot spot is not well known at this time. There are several mechanisms for introducing ablator or fuel material into the hot spot, including various mode hydrodynamic instabilities at the ablation front and fuel-ablator interface, jets from capsule-surface defects, fill tube and target tent in indirect drive, and mounting stalk in direct drive [7,33,49]. Therefore, no one can determine exactly when and how mixing will occur, where mixing will be located, and for how long the mixing will evolve in the implosion. In this work, a hypothesis is proposed that the shell or fuel material mixes into the entire hot-spot area and no clean region exists. Our hot-spot model does not assume an isobaric pressure in the hot-spot region. The

hot-spot density and temperature deviate from the thin-shell model predictions because of mixing, although the thin-shell model has been demonstrated to get good agreement with the LILAC and SPECT3D simulations in Figs. 6 and 8. In this model, it is assumed that the mix is uniformly distributed in order to allow an average atomic mix fraction of CH to D_2; however, the calculation is valid to a good degree even if the CH is strongly localized, provided the pressure and temperature equilibrium conditions are maintained in the hot-spot volume [14,48]. We used this model to investigate the hot-spot temperature, density, and pressure profiles, corresponding to the measured hot-spot x-ray-emissivity profile, and we call this the nonisobaric model.

In a 1D implosion the hot spot is hot enough that the sound speed exceeds the radial flow velocity. This leads to a subsonic hot spot with $\mathrm{Ma}^2 \sim V_i/C_s \ll 1$, where V_i is the implosion velocity and C_s is the sound speed. Under these conditions, the hot spot is isobaric, as shown by scaling each term in the momentum equation $\rho(\partial_t + V\partial_r)V = -\partial_r P$. Since the timescale $t \sim R/V$ and $\partial_r \sim 1/R$ (where R is the hot-spot radius), the left-hand side is of order Ma^2 with respect to the right-hand side and it can be neglected, leading to $\partial_r P \sim 0$ and P uniform (isobaric). In the presence of mix propagating from the hot-spot boundary towards the center, the temperature in the mixed region becomes low enough that the Mach number ($\mathrm{Ma}^2 \sim V^2/t$) is of order unity, the left-hand side of the above equation cannot be neglected, and the hot-spot pressure gradient is finite (nonisobaric hot spot). For example, substituting a linear profile of velocity $V(r,t) = V_i(t)r/R_{\mathrm{HS}}$ into the above equation and assuming a uniform hot-spot density leads to the quadratic pressure profile $P = P(0,t)[1 - \mathrm{Ma}^2(r/R_{\mathrm{HS}})^2(1 + R_{\mathrm{HS}}g/V_i^2)]$, where $P(0,t)$ is the central pressure, Ma is the Mach number defined as $\mathrm{Ma}^2 = \rho V_i^2/2P_0 = m_i V_i^2/2T(1+Z)$, and $g = \partial_t V_i$ is the deceleration (positive because directed in the outward radial direction). The 1D simulation indicates an implosion velocity of 234 km/s and a T_i of 2.8 keV, leading to a Mach number of 0.1 for D_2 and a small deviation from a perfectly isobaric profile. In the presence of mix, the hot-spot temperature decreases to a fraction of a keV and the Mach number becomes of order unity, resulting in a nonisobaric pressure profile.

The fitted hot-spot x-ray-emissivity profile at stagnation is normalized and shown in Fig. 12(a). However, this emissivity profile was from the image plane. The radial hot-spot emissivity distribution was recovered from the inverse Abel transform of the imaged intensity [13] and is shown shown in Fig. 12(a). When compared to the emissivity profile by the analytical thin-shell model, the radial hot-spot emissivity profile has its highest intensity at $\hat{r} = 0.7$, as compared to a peak intensity at the hot-spot boundary in the thin-shell model (and also the LILAC and SPECT3D simulations in Fig. 8). This significant discrepancy is caused by the mixing of the shell material (CH) into the hot-spot region.

Since the isobaric assumption cannot reproduce the measured hot-spot emissivity profile, in our nonisobaric model, in order to recover the measured radial hot-spot emissivity profile, the nonisobaric hot-spot pressure profile at stagnation is assumed to be

$$P(\hat{r}) = P_{\mathrm{HS}}[(1-b)(1-\hat{r}^2)^a + b], \tag{7}$$

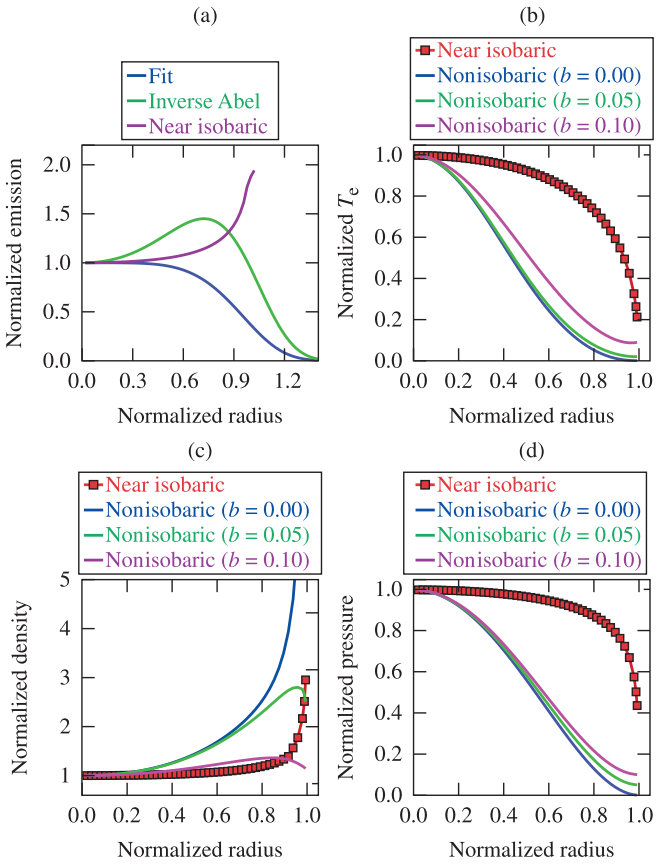

FIG. 12. Hot-spot x-ray-emissivity profile by fitting, the emissivity profile after an inverse Abel transform, and the emissivity profile by the isobaric thin-shell model. (b) Normalized T_e profiles by the thin-shell isobaric model and nonisobaric model with different parameters. (c) Normalized density profiles by the thin-shell isobaric model and nonisobaric model with different parameters. (d) Normalized pressure profiles by the thin-shell isobaric model and nonisobaric model with different parameters. All the x axes are normalized to the hot-spot size of 38 μm at stagnation.

where P_{HS} is the pressure at the target center and a and b are two parameters. With this nonisobaric model, the pressure drops from the hot-spot center ($\hat{r} = 0$) to the hot-spot boundary ($\hat{r} = 1$) and the pressure at $\hat{r} = 1$ is bP_{HS} with $b = 1$ is the isobaric condition. With the above nonisobaric model and bremsstrahlung emissivity formula (6), the hot-spot temperature and density profiles can be straightforward,

$$T_e(\hat{r}) \sim [(1-b)(1-\hat{r}^2)^a + b]^{4/3} I(\hat{r})^{-2/3}, \tag{8}$$

$$\rho(\hat{r}) \sim [(1-b)(1-\hat{r}^2)^a + b]^{-1/3} I(\hat{r})^{2/3}, \tag{9}$$

where $I(\hat{r})$ is the measured hot-spot emissivity profile.

At a sufficiently high spectral energy, typically $h\nu > 3$ keV for implosions on the 60-beam OMEGA laser system, the imploded cores are optically thin and the x-ray measurements are a direct measure of the emissivity, free of absorption and other transport effects [13]. Therefore, the hot-spot emissivity profile obtained by inverse Abel transform can be used directly in the nonisobaric model as $I(\hat{r})$. However, there are two parameters a and b in the nonisobaric model. Here we

use $a = 2$ and $b = 0, 0.05, 0.1$. As has described above, b is the ratio of the hot-spot boundary pressure to the target-center pressure and $b \sim 1$ recovers the isobaric pressure (7). The normalized hot-spot temperature, density, and pressure profiles are presented in Figs. 12(b), 12(c), and 12(d), respectively.

In the previous static model, in the mix region, the shell density decreases linearly from the edge of the mix region to the boundary of the clean region and the temperature decreases linearly from the edge of the clean region to the edge of the mix region. In the clean region, a single temperature and density are assumed [47]. In the refined version of this static model, the density is chosen to be constant in the clean fuel region and to vary linearly in the mixed region and a Gaussian profile is assumed for the temperature [48]. In our nonisobaric model, there is no clean region, the temperature and pressure decrease from the hot-spot center to the boundary, and the density increases from the hot-spot center to the boundary. However, the parameters a and b should be determined experimentally; more work should be performed to investigate the relationship of parameters a and b to the hot-spot absolute emission intensity, the spectrum distribution, the neutron yield, etc. These issues are left for future work.

V. CONCLUSION

In this work, a warm plastic-shell implosion was performed on the OMEGA laser system. The corona plasma was reasonably simulated by the 1D LILAC simulation with nonlocal thermal conduction and CBET models. Good agreement has been achieved with the measured and simulated scattered-laser light spectra, T_e at quarter-critical surface in the corona, and the shell trajectory. The thin-shell model was used to analyze the shell radius evolution in the deceleration phase and is in very good agreement when compared with the LILAC simulation. The SPECT3D-simulated and the thin-shell-model-calculated hot-spot x-ray-emissivity profiles demonstrate that the peak emission intensity occurs at the boundary of the hot spot. The time-dependent hot-spot radius by SPECT3D presents a U-shaped evolution in a 1D clean implosion when the KBFRAMED response is involved. However, a fading-away hot-spot radius evolution was measured in OMEGA warm plastic-shell implosion, because the shell-fuel material mixing into the hot spot causes unstable implosions.

The isobaric hot-spot model is widely used in ICF and its validity relies on the assumption that the hot spot is hot enough that its sound speed exceeds the implosion velocity leading to subsonic flows and therefore flat pressure profiles (isobaric). The isobaric model is widely used to derive hydrodynamic implosion scalings and the relationship of the hot-spot bremsstrahlung emission to the neutron yield and to infer the hot-spot pressure from the neutron yield, ion temperature, burn width, and hot-spot volume.

In this work we have shown that the measured hot-spot emissivity profile at stagnation can be recovered from a nonisobaric model and the normalized hot-spot temperature, density, and pressure profiles are also obtained. The nonisobaric hot-spot model is motivated by the consideration that mixing within the hot spot lowers the sound speed and increases the Mach number. We have shown that the pressure gradient within the hot spot depends on Ma^2, which becomes of order unity in the presence of mix leading to nonisobaric pressure profiles. While the nonisobaric model described in this paper provides a reasonable explanation for the observed self-emission, highly resolved multidimensional simulations of a short-wavelength mix can provide further validation of this model and correlate hot-spot conditions to the hot-spot emission intensity, the emission spectrum distribution, the neutron, and charged-particle spectra. Such 3D simulations will require adaptive mesh refinement to resolve the small-scale mixing driven by the classical unstable interface separating the fuel and the ablator. Additional experiments with Ge or Cu dopants in the ablator can also shed more light on the evolution of the mixing front within the hot spot by measuring time-resolved K-shell emission as described in Ref. [16].

ACKNOWLEDGMENTS

This work was supported by the U.S. Department of Energy under Cooperative Agreements No. DE-FC02-04ER54789 (Office of Fusion Energy Sciences) and No. DE-NA0001944 (National Nuclear Security Administration), by the NYSERDA, by the Presidential Foundation of CAEP (Grant No. YZJJLX 2016007), and by the National Natural Science Foundation of China (Grant No. 11775203). This paper was prepared as an account of work sponsored by an agency of the U.S. Government. Neither the U.S. Government nor any agency thereof, nor any of their employees, makes any warranty, express or implied, or assumes any legal liability or responsibility for the accuracy, completeness, or usefulness of any information, apparatus, product, or process disclosed, or represents that its use would not infringe privately owned rights. The views and opinions of authors expressed herein do not necessarily state or reflect those of the U.S. Government or any agency thereof.

[1] J. Lindl, P. Amendt, R. Berger, S. Glendinning, S. Glenzer, S. Haan, R. Kauffman, O. Landen, and L. Suter, Phys. Plasmas **11**, 339 (2004).

[2] R. Betti and O. A. Hurricane, Nat. Phys. **12**, 435 (2016).

[3] M. Lafon, R. Betti, K. S. Anderson, T. J. B. Collins, R. Epstein, P. W. McKenty, J. F. Myatt, A. Shvydky, and S. Skupsky, Phys. Plasmas **22**, 032703 (2015).

[4] V. N. Goncharov *et al.*, Plasma Phys. Controlled Fusion **59**, 014008 (2017).

[5] S. P. Regan *et al.*, Phys. Rev. Lett. **117**, 025001 (2016).

[6] S. W. Haan *et al.*, Phys. Plasmas **18**, 051001 (2011).

[7] N. B. Meezan *et al.*, Plasma Phys. Controlled Fusion **59**, 014021 (2017).

[8] J. Lindl, O. Landen, J. Edwards, E. Moses, and NIC Team, Phys. Plasmas **21**, 129902(E) (2014).

[9] W. L. Shang, R. Betti, S. X. Hu, K. Woo, L. Hao, C. Ren, A. R. Christopherson, A. Bose, and W. Theobald, Phys. Rev. Lett. **119**, 195001 (2017).

[10] M. J. Edwards *et al.*, Phys. Plasmas **18**, 051003 (2011).

[11] S. X. Hu, V. N. Goncharov, P. B. Radha, J. A. Marozas, S. Skupsky, T. R. Boehly, T. C. Sangster, D. D. Meyerhofer, and R. L. McCrory, Phys. Plasmas **17**, 102706 (2010).

[12] H. R. Griem, *Principles of Plasma Spectroscopy* (Cambridge University Press, Cambridge, 1997).

[13] R. Epstein, V. N. Goncharov, F. J. Marshall, R. Betti, R. Nora, A. R. Christopherson, I. E. Golovkin, and J. J. MacFarlane, Phys. Plasmas **22**, 022707 (2015).

[14] T. Ma *et al.*, Phys. Rev. Lett. **111**, 085004 (2013).

[15] S. P. Regan *et al.*, Phys. Plasmas **19**, 056307 (2012).

[16] S. P. Regan *et al.*, Phys. Rev. Lett. **111**, 045001 (2013).

[17] J. A. Baumgaertel, P. A. Bradley, S. C. Hsu, J. A. Cobble, P. Hakel, I. L. Tregillis, N. S. Krasheninnikova, T. J. Murphy, M. J. Schmitt, R. C. Shah, K. D. Obrey, S. Batha, H. Johns, T. Joshi, D. Mayes, R. C. Mancini, and T. Nagayama, Phys. Plasmas **21**, 052706 (2014).

[18] T. C. Sangster *et al.*, Phys. Plasmas **20**, 056317 (2013).

[19] T. Ma *et al.*, Phys. Plasmas **24**, 056311 (2017).

[20] J. J. MacFarlane, I. E. Golovkin, P. Wang, P. R. Woodruff, and N. A. Pereyra, High Energy Density Phys. **3**, 181 (2007).

[21] J. Delettrez, R. Epstein, M. C. Richardson, P. A. Jaanimagi, and B. L. Henke, Phys. Rev. A **36**, 3926 (1987).

[22] R. Betti and C. Zhou, Phys. Plasmas **12**, 110702 (2005).

[23] T. R. Boehly, V. A. Smalyuk, D. D. Meyerhofer, J. P. Knauer, D. K. Bradley, R. S. Craxton, M. J. Guardalben, S. Skupsky, and T. J. Kessler, J. Appl. Phys. **85**, 3444 (1999).

[24] Y. Lin, T. J. Kessler, and G. N. Lawrence, Opt. Lett. **21**, 1703 (1996).

[25] S. Skupsky, R. W. Short, T. Kessler, R. S. Craxton, S. Letzring, and J. M. Soures, J. Appl. Phys. **66**, 3456 (1989).

[26] I. V. Igumenshchev, D. H. Edgell, V. N. Goncharov, J. A. Delettrez, A. V. Maximov, J. F. Myatt, W. Seka, A. Shvydky, S. Skupsky, and C. Stoeckl, Phys. Plasmas **17**, 122708 (2010).

[27] I. V. Igumenshchev *et al.*, Phys. Plasmas **19**, 056314 (2012).

[28] V. N. Goncharov *et al.*, Phys. Plasmas **21**, 056315 (2014).

[29] W. Seka, D. H. Edgell, J. P. Knauer, J. F. Myatt, A. V. Maximov, R. W. Short, T. C. Sangster, C. Stoeckl, R. E. Bahr, R. S. Craxton, J. A. Delettrez, V. N. Goncharov, I. V. Igumenshchev, and D. Shvarts, Phys. Plasmas **15**, 056312 (2008).

[30] C. D. Zhou and R. Betti, Phys. Plasmas **14**, 072703 (2007).

[31] R. K. Kirkwood, J. D. Moody, J. Kline, E. Dewald, S. Glenzer, L. Divol, P. Michel, D. Hinkel, R. Berger, E. Williams, J. Milovich, L. Yin, H. Rose, B. MacGowan, O. Landen, M. Rosen, and J. Lindl, Plasma Phys. Controlled Fusion **55**, 103001 (2013).

[32] W. Seka, D. H. Edgell, J. F. Myatt, A. V. Maximov, R. W. Short, V. N. Goncharov, and H. A. Baldis, Phys. Plasmas **16**, 052701 (2009).

[33] R. S. Craxton *et al.*, Phys. Plasmas **22**, 110501 (2015).

[34] C. Stoeckl, W. Theobald, S. P. Regan, and M. H. Romanofsky, Rev. Sci. Instrum. **87**, 11E323 (2016).

[35] R. P. Drake, R. E. Turner, B. F. Lasinski, E. A. Williams, K. Estabrook, W. L. Kruer, E. M. Campbell, and T. W. Johnston, Phys. Rev. A **40**, 3219 (1989).

[36] D. T. Michel, A. K. Davis, W. Armstrong, R. Bahr, R. Epstein, V. N. Goncharov, M. Hohenberger, I. V. Igumenshchev, R. Jungquist, D. D. Meyerhofer, P. B. Radha, T. C. Sangster, C. Sorce, and D. H. Froula, High Power Laser Sci. Eng. **3**, e19 (2015).

[37] D. T. Michel, R. S. Craxton, A. K. Davis, R. Epstein, V. Y. Glebov, V. N. Goncharov, S. X. Hu, I. V. Igumenshchev, D. D. Meyerhofer, P. B. Radha, T. C. Sangster, W. Seka, C. Stoeckl, and D. H. Froula, Plasma Phys. Controlled Fusion **57**, 014023 (2015).

[38] A. K. Davis, D. T. Michel, R. S. Craxton, R. Epstein, and M. Hohenberger, Rev. Sci. Instrum. **87**, 11E340 (2016).

[39] C. Stoeckl, V. Y. Glebov, S. Roberts, T. C. Sangster, R. A. Lerche, R. L. Griffith, and C. Sorce, Rev. Sci. Instrum. **74**, 1713 (2003).

[40] W. Theobald *et al.*, Phys. Plasmas **15**, 056306 (2008).

[41] R. Betti, M. Umansky, V. Lobatchev, V. N. Goncharov, and R. L. McCrory, Phys. Plasmas **8**, 5257 (2001).

[42] F. J. Marshall, R. E. Bahr, V. N. Goncharov, V. Y. Glebov, B. Peng, S. P. Regan, T. C. Sangster, and C. Stoeckl, Rev. Sci. Instrum. **88**, 093702 (2017). .

[43] J. D. Lindl, *Inertial Confinement Fusion: The Quest for Ignition and Energy Gain Using Indirect Drive* (Springer, New York, 1998).

[44] J. R. Rygg, Ph.D. thesis, Massachusetts Institute of Technology, 2006.

[45] S. H. Glenzer *et al.*, Plasma Phys. Controlled Fusion **54**, 045013 (2012).

[46] C. Cerjan, P. T. Springer, and S. M. Sepke, Phys. Plasmas **20**, 056319 (2013).

[47] D. D. Meyerhofer *et al.*, Phys. Plasmas **8**, 2251 (2001).

[48] P. B. Radha *et al.*, Phys. Plasmas **9**, 2208 (2002).

[49] B. A. Hammel, H. A. Scott, S. P. Regan, C. Cerjan, D. S. Clark, M. J. Edwards, R. Epstein, S. H. Glenzer, S. W. Haan, N. Izumi, J. A. Koch, G. A. Kyrala, O. L. Landen, S. H. Langer, K. Peterson, V. A. Smalyuk, L. J. Suter, and D. C. Wilson, Phys. Plasmas **18**, 056310 (2011).